Wavelength-dependent ripple propagation on ion-irradiated prepatterned surfaces driven by viscous flow corroborates two-field continuum model

Detlef Kramczynski,[1] Bernhard Reuscher,[2] and Hubert Gnaser[1,2,*]

[1]*Fachbereich Physik and Forschungszentrum OPTIMAS, Technische Universität Kaiserslautern, D-67663 Kaiserslautern, Germany*

[2]*Institut für Oberflächen- und Schichtanalytik GmbH (IFOS), Trippstadter Str. 120, D-67663 Kaiserslautern, Germany*

Glass surfaces were patterned by milling periodic trench structures with wavelengths from 150 to 750 nm in a focused ion-beam (FIB) system. Upon exposure to 30 keV Ga$^+$ ion irradiation under an incidence angle of 52° with respect to the surface normal, those patterns were found to transform into "ripple"-like nanostructures. Their evolution was monitored *in situ* for ion fluence from 5×10^{16} to 2.4×10^{18} Ga$^+$ ions/cm^2 using the scanning electron microscope incorporated in the FIB. With increasing fluence, the wavelengths of the ripples remain constant (and equal to their original feature size) while they propagate across the surface, in a direction which coincides with the projection of the ion beam's incident direction onto the surface. The propagation velocities v, being in the range $(60-100)$ nm/(10^{17} ions cm^{-2}), were determined to be inversely proportional to the wavelengths λ, with $v = A + B/\lambda^2$ (the constants A and B derive from various ion beam and target material parameters). Such a dependence is in accordance with the predictions of a theoretical two-field continuum model of ripple formation which treats the surface as being composed of a thin layer of mobile species on the substrate. A quantitative agreement of the experimental findings with this model is obtained if the presence of a viscous flow is effective in that thin surface layer. *Ex situ* atomic force microscopy was employed to derive the final crest-to-valley amplitudes of the ripple structures; their values were $\sim 50-100$ nm and thus similar to the depth of the original trenches. On the pristine surface areas (which have not been patterned), ripples were also formed by ion bombardment. Their wavelength increases with ion fluence Φ from ~ 250 to ~ 420 nm, following a dependence $\lambda \propto \Phi^{0.19}$.

I. INTRODUCTION

The irradiation of solid surfaces by energetic particles leads to a variety of phenomena that are closely correlated with the energy deposition processes of the incoming ions [1,2]. At the surface, ion irradiation may result in substantial morphological changes [3]. At low fluences, isolated defects such as vacancies and adatoms may be created [4]. If these defects are mobile (for example, at elevated sample temperatures), they may annihilate or form adatom and vacancy clusters. For higher bombarding fluences, such structures may result in a coarsening of the surface; the extent of this roughening may depend on the specimen temperature. Eventually, prolonged ion bombardment often leads to the development of a very specific surface morphology. Interestingly, these structures can have highly periodic features, such as "nanodots" [5,6] or "ripple"-like contours [7,8], with feature sizes in the nanometer range. These self-organized nanostructures evolving due to ion irradiation on surfaces have been studied quite thoroughly in the past decade [9–14].

Generally, the formation of these structures is assumed to be related to (and caused by) the interplay between ion erosion (which roughens the surface) and transport processes (diffusion) which induce a smoothing [10,11,13]. The evolution of ripples during ion sputtering is caused by an ion-induced instability: valleys are eroded faster than crests. This instability is balanced by surface diffusion; hence, a competition between roughening (curvature-dependent erosion) and smoothing exists, while other processes, such as beam-enhanced surface

diffusion [15,16] or viscous flow [17,18] within the ion penetration layer, could also contribute.

Theoretically, a substantial degree of understanding of ripple formation is due to the pioneering model proposed by Bradley and Harper (BH) [19] that considers the surface evolution in terms of the dynamic balance between roughening and smoothing processes. The concept of BH combines the effects of sputtering and surface diffusion and is based on the sputtering theory of Sigmund [20,21]. The latter relates the rate of atom removal to the energy deposited by the incident ion in the near-surface region in a sequence of collisions. Bradley and Harper extended that approach and emphasized that the sputtering yield is proportional to the curvature of the surface; eventually, this may lead to a roughening. This process could be balanced by surface relaxation which depends on the divergence of the surface curvature. Combining these competitive mechanisms, BH derived an equation for the surface height $h(x,y,t)$ [10,19]

$$\frac{\partial h}{\partial t} = -v_0 + \frac{\partial v_0}{\partial \theta}\frac{\partial h}{\partial x} + v_x \frac{\partial^2 h}{\partial x^2} + v_y \frac{\partial^2 h}{\partial y^2} - K\nabla^4 h. \quad (1)$$

Here, v_0 is the average erosion velocity of the surface which depends on the incidence angle of the ion beam θ, the ion flux, and the sputtering yield. Also, v_x and v_y are functions of the ion-beam parameters [10] and relate the sputtering yield at any point on the surface to the local curvature. The last term in Eq. (1) represents surface diffusion of mobile species and is proportional to the divergence of the curvature [22,23]. The parameter K depends on the surface energy, the diffusivity of mobile surface defects, and their average concentration. A similar functional form of smoothing can arise from

*Corresponding author: gnaser@rhrk.uni-kl.de

ion-induced viscous flow in the surface layer [24] and ion-induced diffusion [9]. Several extensions and modifications of the BH model were later envisaged [10]. For example, the inclusion, in Eq. (1), of nonlinear terms of the surface curvature was proposed [25], as well as a noise term which takes into account the stochastic arrival of ions. Alternative mechanisms of surface relaxation, such as ion-induced and thermally induced stress [26], ion-induced anisotropic plastic flow [27,28], hydrodynamic [29–31], or others processes [32,33], were pointed out. Furthermore, the possible contribution of mass distribution by ion bombardment was emphasized [34–36]. In fact, recent work by Aziz *et al.* [37,38] has shown that this mechanism can have a decisive if not dominant influence on the evolution of ripples, to the extent that the erosive effect is essentially irrelevant. In addition, the Gaussian distribution of energy deposition original proposed by Sigmund [21] might require a further refinement. Several recent publications reported attempts to compute such energy distributions via molecular dynamics simulations [39–41].

Equation (1) predicts that each Fourier component of the surface height will grow exponentially with a rate that depends on the wavevector, and a maximum growth rate might be reached. The corresponding modulation will outgrow the others and lead to ripples with a characteristic wavelength λ^*

$$\lambda^* = 2\pi \sqrt{2K / v_{\max}}, \tag{2}$$

where $v_{\max}$ is the maximum of the two values v_x and v_y in Eq. (1). The magnitude of the latter determines the orientation of the ripple pattern with respect to the ion-beam direction [19].

An intriguing albeit not completely resolved question is whether these surface features possibly exhibit a lateral movement (i.e. a propagation parallel to the global surface) with increasing ion fluence. The BH concept and related models predict a movement of ripples on a surface bombarded by ions under an oblique incidence angle. In the approximation of small surface slopes, the ripples with a wavevector parallel to the beam will travel at a rate [19]

$$v = -v_0 \left(\frac{1}{Y(\theta)} \frac{dY}{d\theta} - \tan\theta \right), \tag{3}$$

where $Y(\theta)$ is the sputtering yield of the target. Up to fairly large values of θ ($\sim 70°$), the propagation of ripples should occur in a negative direction, that is, opposite to that of the ion-beam projection onto the surface. Previous experimental observations [42–49] have generally shown a ripple propagation in a positive direction, contrary to Eq. (3). In these studies, a rather narrow range of propagation velocities, $\sim (40-80)$ nm/10^{17} ions cm^{-2} was found despite the considerable variety of targets and ion-bombardment conditions that were employed. However, a recent experiment by Hofsäss *et al.* [49] demonstrated that the direction might actually switch at a specific incidence angle. They investigated 10 keV Xe$^+$ bombardment of Si in a narrow range of θ ($62°-70°$) and found a positive ripple movement for $\theta \geq 67°$, whereas it is negative for $\theta \leq 67°$. Interestingly, this reversal occurs over an extremely small range of $\Delta\theta \sim 1°$ (somewhat surprisingly, this work claims an angular spread of the ion beam of below $1°$ despite the fact that the ion beam was swept over an area of 10 mm). The propagation of ripples has been found also in

Monte Carlo computer simulations [50–52]. Contrary to the experimental data, computer simulations of ripple formation and dynamics appear to indicate that, under oblique ion incidence, ripples propagate along a direction opposite to that of the ion beam.

Apart from the discrepancies associated with the direction of propagation, a possible dependence of the propagation velocity on the ripple wavelength has not been examined. The BH theory and similar ones do not predict such a dependence, see Eq. (3). In order to resolve this issue, in this paper, periodic patterns were fabricated on the surface before ion irradiation. The idea was to select *a priori* specific wavelengths and to monitor their propagation with increasing fluence, thereby possibly deriving a velocity-versus-wavelength relation. The evolution of prepatterned periodic structure(s) on surfaces under ion bombardment has actually been studied with the objective to achieve more diverse nanostructures with improved control over the pertinent process; it has been proposed to fabricate nanopatterns by multiple ion-beam sputtering, in which more than one ion beam is directed onto a surface, either simultaneously [53] or sequentially [54–58]. Generally, quite diverse nanostructures may evolve under these conditions.

The objective of this paper was hence twofold: (i) selecting on the surface ripples with specific wavelengths by using prepatterned periodic structures, and (ii) examining the movement of these ripples under ion bombardment as a function of ion fluence. In this way, a possible dependence of the propagation velocity on the ripple wavelength could thereby be determined. To achieve this goal, a focused ion-beam (FIB) system was employed: this dual-beam instrument features a finely focused Ga$^+$ ion beam and a scanning electron microscope (SEM). The surface was irradiated by 30 keV Ga$^+$ ions (incidence angle $\theta = 52°$) and, without sample movement, the area hit by the ions could be monitored *in situ*. Taking SEM images at different ion fluences, the movement of the ripples could be observed and the propagation velocity was determined.

II. EXPERIMENTAL

The 30-keV Ga$^+$ ion bombardments were carried out using a dual-beam FIB system (Altura 875, FEI), consisting of a highly focused Ga$^+$ ion beam and a scanning electron microscope (SEM). The geometrical angle between ion and electron beam is $52°$. The Ga$^+$ beam was used both for initially milling the periodic structures and for subsequently bombarding these patterns. For the latter, SEM images of the ion-bombarded area were recorded at fluence increments of 3×10^{16} ions/cm^2 without moving the sample (the incidence angle of the electron beam was then perpendicular to the surface). The total irradiation fluence amounted to 2.4×10^{18} ions/cm^2.

The surface topography present upon the completion of ion bombardment was investigated *ex situ* by atomic force microscopy (AFM) (Dimension 5000R, Veeco) in the tapping mode (frequency ~ 170 kHz, nominal force constant ~ 50 N/m, scan rate 0.3 Hz).

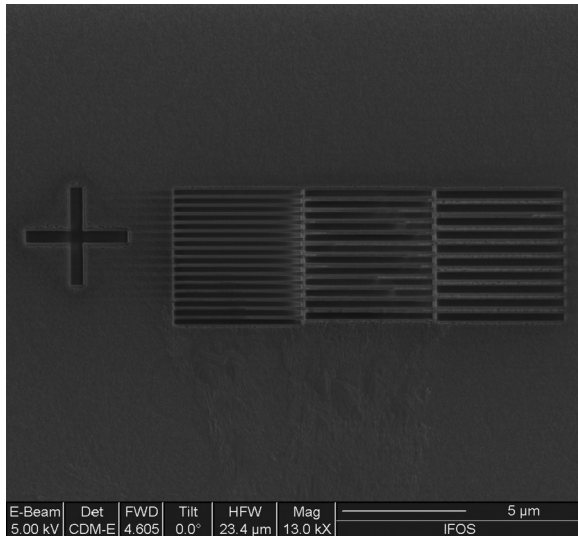The target material used for this study was soda-lime glass (microscope slides). To minimize charging during ion

FIG. 1. Scanning electron microscope image of periodic structures on the surface fabricated by FIB (30 keV Ga$^+$, $\theta = 0°$). They consist of three series of trenches (each 5 μm wide and 100 nm deep) milled into the sample separated by distances (wavelengths) of $\lambda_p =$ 350, 450, and 550 nm, respectively. The cross at the left serves as a reference position.

or electron irradiation, the sample surface was covered with a thin (10 nm) Au layer.

III. RESULTS

A. Prepatterned surface

In order to investigate the possible influence of an existing periodic surface structure on the selection and evolution of a specific wavelength for ripples under ion bombardment, the FIB was employed to fabricate such periodic patterns (30 keV Ga$^+$ ions, $\theta = 0°$). They consisted of several series of trenches (each 5 μm wide and 100 nm deep) milled into the sample separated by distances such that their cross-sectional profile corresponds to rectangular oscillations with wavelengths of $\lambda_p = $ 150, 250, 350, 450, 550, 650, and 750 nm, respectively; this resulted in 36, 22, 16, 12, 10, 9, and 8 trenches for these λ_p. These values of λ_p were chosen to bracket the ripple wavelength of $\sim$450 nm found on a pristine glass surface in a previous study [48]. In addition, a cross was sputtered into the sample which served as a reference mark in the following irradiation experiments (and which was not hit by the ion beam). Figure 1 is an SEM image showing such patterns for $\lambda_p = $ 350, 450, and 550 nm.

This structuring process will lead to a saturated Ga concentration in the bottom of the trenches while the top surfaces will initially be free of Ga. While the actual Ga concentration is not known, a previous study [59] would indicate that, for the present irradiation conditions, the Ga content might amount to 10−15% in a near-surface layer of about 10 nm. However, the Ga-free areas will be rapidly saturated also with Ga during the subsequent irradiation experiments. The fluence to reach this stationary state is estimated to amount to $\sim 1 \times 10^{17}$ cm^{-2} [59] which constitutes only a very small fraction of the total bombarding fluence. Some (small) lateral inhomogeneities in

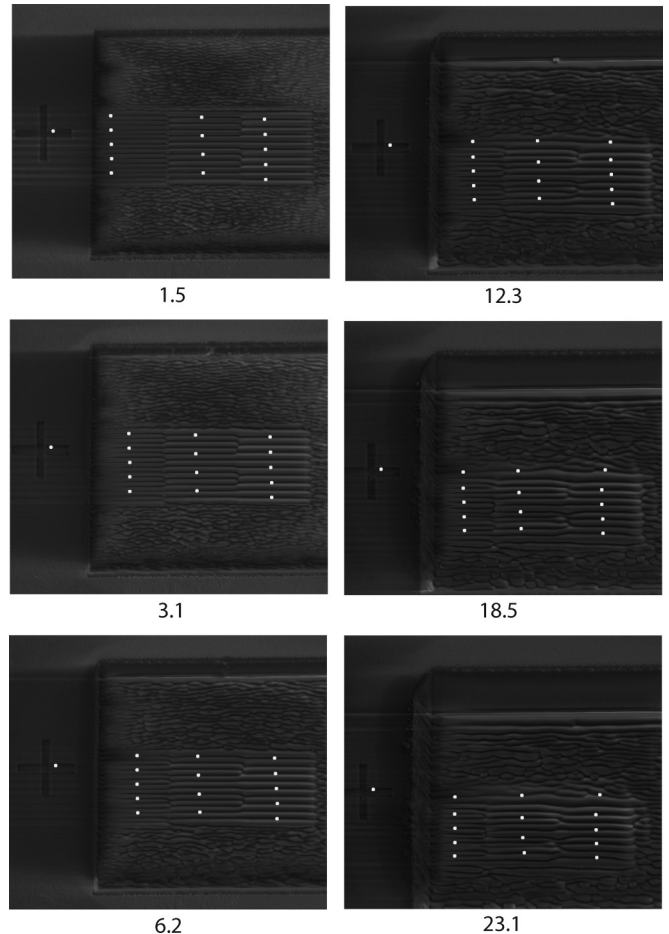FIG. 2. Scanning electron microscope micrographs (23 × 20) μm^2 of the ripple structure on the prepatterned surface (Fig. 1) bombarded by 30 keV Ga$^+$ ions in the FIB. The ions' incidence angle was 52°, and the incidence direction was from the top. The images were taken with the scanning electron microscope *in situ* in the FIB at the specified fluences (given in 1×10^{17} cm^{-2}). The white dots mark the positions of individual ripples and are used to monitor the ripple propagation with fluence; they are referenced to the cross which is not bombarded. With increasing fluence, the images show that the ripples move towards the bottom.

the Ga distribution may arise from the different angle at which the ion beam hits the evolving ripples.

These prepatterned structures were bombarded by 30 keV Ga$^+$ ions ($\theta = 52°$) with an ion flux (density) $f = 3.1 \times 10^{14}$ cm^{-2} s^{-1}. The irradiated area was chosen in a way to include in addition parts of the surrounding surface in order to monitor the ripple evolution also in these pristine (nonpatterned) regions. The ion fluence Φ was increased in increments of 3×10^{16} Ga$^+$ ions cm^{-2}; an SEM micrograph was recorded after each irradiation step, imaging the area hit by the ions without sample movement. Figure 2 shows a series of such SEM micrographs of the patterned surface ($\lambda_p = $ 350, 450, and 550 nm) irradiated by the Ga$^+$ ions. The numbers beneath the images give the fluences Φ (in 1×10^{17} cm^{-2}). The incidence direction of the Ga$^+$ beam is from the top. The white dots mark specific features in the prepatterned structures, and their movement relative the dot at the cross (which is not
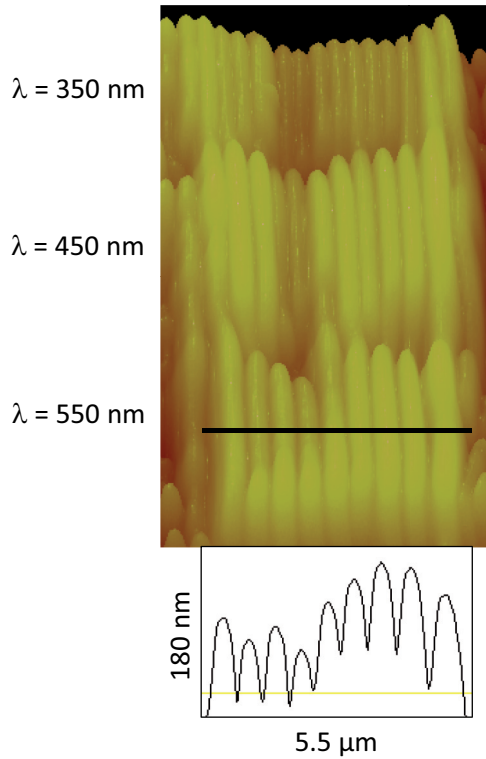
FIG. 3. (Color online) Atomic force microscopy topographic image of the ripple structures on the surface originally patterned with $\lambda_p = 350$, 450, and 550 nm (as in Fig. 1, but rotated clockwise by 90°). The image was taken upon completion of the ion irradiation (corresponding to an accumulated fluence of 2.4×10^{18} ions cm^{-2}). The direction of the ion beam is from the right, and the surface is viewed at an angle of 50°. The profile given in the lower part is a cross section in the 550-nm structure along the marked line.
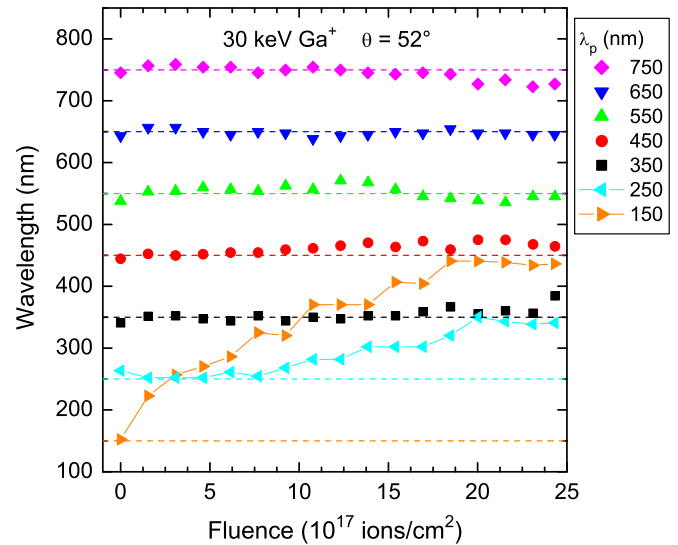

FIG. 4. (Color online) The wavelengths of the ripple structures (with $\lambda_p = 150-750$ nm) are plotted as a function of the ion fluence. The horizontal lines indicate the original values of the periodic structures.

bombarded) is used to determine the propagation velocity of the ripples. It is clearly seen that, over the irradiation sequence, the dots move towards the bottom, that is, in the direction of the projection of the incident ion beam. This direction of propagation is in agreement with previous studies.

Outside of the prestructured areas (i.e. on the pristine surface), ripple formation is found to start at a fluence of $\sim 5 \times 10^{16}$ cm^{-2}. While some of the smaller features appear to coalesce into larger ones with increasing fluence, a close inspection of the SEM images indicates that these (pristine) ripples also propagate in the direction of the incident ion beam (towards the bottom in Fig. 2). The wavelength of these ripples is found to grow with increasing fluence (this will be discussed below).

Upon completion of the irradiation in the FIB, this specimen was investigated *ex situ* by AFM in order to inspect the final ripple amplitudes. Figure 3 shows an AFM micrograph of the surface originally patterned with $\lambda_p = 350$, 450, and 550 nm (Fig. 1) and bombarded by an accumulated fluence of 2.4×10^{18} cm^{-2}. The view is under an angle of 50°, visualizing the ripple profiles. From line scans across the ripple structures the average crest-to-valley amplitudes was evaluated and found to be in the range $50-100$ nm for the different λ_p. These values are thus very close to the original depth of the trenches (100 nm). The total depth of the crater eroded at $\Phi = 2.4 \times$

10^{18} cm^{-2} as determined from the AFM data was ~ 1.4 μm; from this, a sputtering yield of ~ 4.2 atoms/Ga$^+$ ion is derived.

The SEM images in Fig. 2 indicate already that the wavelengths of the ripples that evolve from the prepatterned structures stay essentially constant with continuing ion bombardment. The average wavelengths of the patterns with original $\lambda_p = 150-750$ nm were evaluated using all ripples (not only the ones with a white dot) and are plotted as a function of ion fluence in Figure 4. The data show that the wavelengths of the ripples which form from the original structures with $\lambda_p \geq 350$ nm are essentially independent of fluence and remain equal to λ_p. Equation (2) predicts that, on an undisturbed (flat) surface, a characteristic wavelength will evolve; this is actually observed on the pristine surfaces (see below). On the other hand, selecting such a wavelength *a priori* (here, by the patterns with specific λ_p), it apparently will dominate the ripple evolution during ion irradiation.

The patterns with $\lambda_p = 150$ and 250 nm deviate from this trend: here, the ripple wavelengths increase with Φ. This effect is particularly pronounced for the $\lambda_p = 150$ nm structure and is also visible in the corresponding SEM images which show that the trenches are rapidly blurred upon ion bombardment. A possible reason for this discrepancy could be due to shadowing effects: because of the ions' incidence angle (52°) a 128-nm-wide part of the bottom of the trenches (which are 100 nm deep) is not hit by the ions. Hence, for the $\lambda_p = 150$ nm structures, only a very small fraction of the bottom area is therefore eroded, and the preselection of a specific wavelength, as seen for $\lambda_p \geq 350$ nm, may not be effective in this case. The wavelength of the ripples is found to approach a limiting value of $\lambda \sim 440$ nm which is essentially identical with that on the flat surface (see below). The $\lambda_p = 250$ nm structures might constitute an intermediate case: over a considerable fluence range, the wavelength remains equal to λ_p, but some coarsening is observed before the wavelength
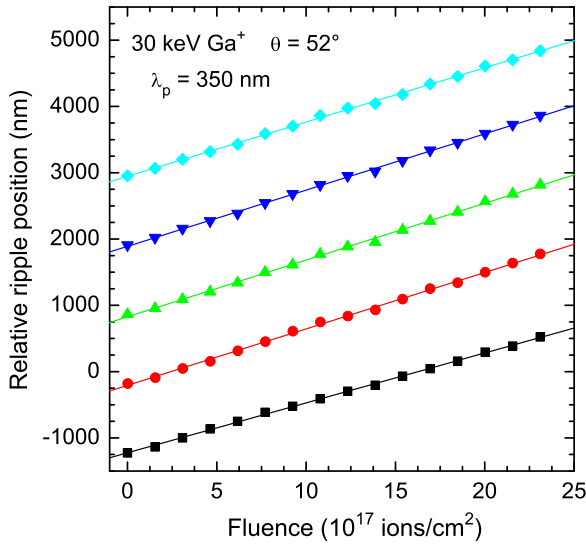
FIG. 5. (Color online) The relative positions of the ripple structures (with $\lambda_p = 350$ nm) are plotted as a function of the ion fluence. The straight lines are fits to the data; their slopes correspond to the propagation velocity of the ripples. From top to bottom, their values are: 81.9 ± 0.7, 84.9 ± 0.6, 85.6 ± 0.8, 85.1 ± 0.8, and 75.3 ± 0.5 nm/(10^{17} ions cm^{-2}).
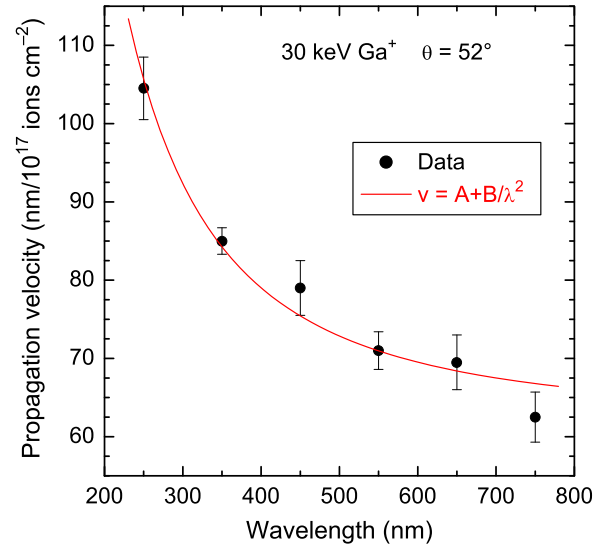

FIG. 6. (Color online) The propagation velocities of the ripples that formed on the patterned structures (Fig. 2) are plotted as a function of their respective wavelengths. The solid line is a fit according to $v = A_{exp} + B_{exp}/\lambda^2$, giving $A_{exp} = (61.9 \pm 1.9)$ nm/(10^{17} ions cm^{-2}) and $B_{exp} = (2.73 \pm 0.24) \times 10^6$ nm^3/(10^{17} ions cm^{-2}). The fit yields a reduced $\chi^2 = 8.6$ and $R^2 = 0.97$.

reaches a stationary level (~ 340 nm); this is lower, however, than that for the pristine surface.

From the complete series of SEM images taken during the irradiation (up to $\Phi = 2.4 \times 10^{18}$ Ga$^+$ ions/cm^2), the relative positions of selected features in the prepatterned structures (the white dots in Fig. 2) were determined with respect to the stationary mark at the cross. Figure 5 depicts these values as a function of the ion fluence for the case of $\lambda_p = 350$ nm. The data for all five positions show a linear correlation with the ion fluence, and the slopes of the linear fits (straight lines) give the propagation velocity. The same behavior was observed also for the structures with other λ_p. However, the propagation velocity was found to decrease with increasing λ_p.

More specific effects appear to evolve in the regions where the prepatterned and pristine areas meet; here, conflicting wavelengths may exist. In these border regions, ripples tend to change their wavelengths with time which renders velocity measurements useless as both shifts overlap; these data have not been used in this paper. However, it has been observed previously that the ripple pattern resulting from irradiation may be influenced by the boundary condition of the irradiated region [46,60,61].

The propagation velocity v of ripples was determined from the linear correlation between the relative ripple positions and the fluence (cf. Fig. 5). These data are summarized in Figure 6 which shows the propagation velocities as a function of wavelength for the patterned structures. The velocity of ripple propagation is found to decrease monotonously with increasing ripple wavelength, falling from ~ 105 to ~ 60 nm/10^{17} ions cm^{-2} for λ between 250 and 750 nm. These values are in the range determined in a previous experiment on a nonpatterned surface ($v \sim 77$ nm/10^{17} cm^{-2} [48]). The data have been fitted by a function $v = A_{exp} + B_{exp}/\lambda^2$ (solid line in Fig. 6), resulting in values of $A_{exp} =$

(61.9 ± 1.9) nm/(10^{17} ions cm^{-2}) and $B_{exp} = (2.73 \pm 0.24) \times 10^6$ nm^3/(10^{17} ions cm^{-2}). The justification for using this specific fitting function is due to a theoretical concept discussed in the next section.

B. Pristine surface

The ripple evolution on the pristine surface (the areas which have not been patterned) was examined as a function of ion fluence from the SEM images, and the wavelength was determined from the area located above the structured pattern in Fig. 2, analyzing the greyscale images with a two-dimensional autocorrelation function. Using a series of SEM images, the average wavelength of the ripples is found to increase with ion fluence, from $\lambda = 250$ to 420 nm. This dependence is depicted in Figure 7. The solid line is a fit to the data according to $\lambda \propto \Phi^{0.19 \pm 0.004}$. Ripple coarsening following such a power-law dependence has been observed before, but a number of different values of the exponent were reported [14]. Velocity measurements in this case are more difficult because of the changing wavelength, and in addition, these ripples are less regular than the artificial ones on the prepatterned areas, and they tend to change their shapes with irradiation time. Nevertheless, for ripples with $\lambda \sim 500$ nm, a propagation velocity $v \sim 73$ nm/10^{17} ions cm^{-2} was derived which fits quite well to the data in Fig. 6. Furthermore, the direction of the propagation was clearly along the projection of the ion beam on the surface, in agreement with the prepatterned ripples and previous studies [42,44,48].

IV. DISCUSSION

The results illustrate that (i) the selection of specific ripple wavelengths is possible by prepatterning the surface with
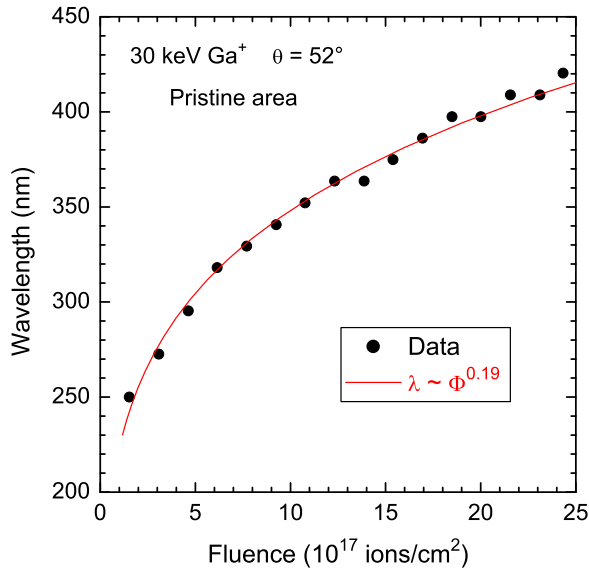
FIG. 7. (Color online) The wavelength of ripples that formed on the pristine surface is plotted as a function of the ion fluence. The wavelength was determined from the area above the periodic patterns (upper half of the irradiated region in Fig. 2). The solid line is a fit of the data with $\lambda \propto \Phi^{0.19\pm0.004}$.

corresponding structures, (ii) these ripple propagate across the surface in a direction coinciding with that of the ion beam, and (iii) their propagation velocity scales inversely with the wavelength, with $v = A_{exp} + B_{exp}/\lambda^2$. It has been mentioned in Sec. I that the BH theory does not predict the propagation direction observed in this and previous experiments; furthermore, a dependence of the velocity v on the wavelength λ, as observed in Fig. 6, is not explicitly included in it. Other theoretical concepts that go beyond BH have been proposed (for a detailed discussion, see, for example, [10,13,14]); their predictions in terms of ripple propagation direction and velocity will be examined in the following and compared with present results.

A. Two-field continuum model of ripple formation

Typically, in these continuum models a single evolution equation is formulated for the surface height field $h(\mathbf{r},t)$, and contributions to such equations are resulting from the various relaxation mechanisms influencing surface topography (one- or single-field models). Following a previous approach [62,63], Cuerno *et al.* [29,30,64–66] proposed a model to describe the temporal evolution of the topography employing two coupled fields, namely the density of mobile species being transported at the surface and the local height of the static target. A key ingredient is the formation of a thin amorphous layer at the target surface through irradiation; in such a thin viscous layer, material transport onto the eroded target could be (strongly) enhanced [64]. The surface dynamics can be completely described through the time evolution of these two fields: the height $h(\mathbf{r}, t)$ of the static substrate at time t and point $\mathbf{r} = (x, y)$ on a reference plane that coincides with the noneroded flat surface and the thickness $R(\mathbf{r}, t)$ of the thin surface layer of mobile species [64]. This approach

predicts a dependence of the ripple propagation velocity on the wavelength which can be compared in a quantitative way with the experimental findings (Fig. 6). This two-field model has already successfully explained in a quantitative way the dynamics of a nanodot pattern induced on silicon surfaces with simultaneous metal codeposition [67].

In the model proposed by Muñoz-Garcia, Cuerno, and Castro (MCC) [29,30,64], the dynamics of the two fields are coupled via [64]

$$\frac{\partial R}{\partial t} = (1 - \varphi) \cdot \Gamma_{ex} - \Gamma_{ad} - \vec{\nabla} \cdot \vec{J},$$
$$\frac{\partial h}{\partial t} = -\Gamma_{ex} + \Gamma_{ad}. \tag{4}$$

Atoms can move back and forth between those layers. Here, Γ_{ex} is the velocity by which material is excavated from the immobile target due to irradiation (locally decreasing the value of h), and Γ_{ad} is the rate at which mobile material is incorporated back into the immobile bulk (locally increasing the value of h). Atoms from the static layer enter the dynamic layer by receiving part of the energy an ion impact deposited into the surface, but only a fraction φ $(0 \leq \varphi \leq 1)$ of the atoms is sputtered away. A fraction $(1 - \varphi)$ stays in the dynamic layer and leads to growth of that layer. This process models redeposition. The surface relaxation is described by a flux **J** of atoms moving laterally on the surface.

The rate at which atoms are sputtered depends principally on the specific experimental parameters used; these will determine the distribution of energy deposition. Going beyond Sigmund's Gaussian distribution originally applied by BH [19], MCC developed the local erosion velocity at a location $h(\mathbf{r},t)$ in terms of a rather general distribution function [64]

$$\Gamma_{ex} = \alpha_0 \Bigg[1 + \alpha_{1x} \frac{\partial h}{\partial x} + \vec{\nabla} \cdot (\underline{\alpha_2} \cdot \vec{\nabla} h) + \frac{\partial \vec{\nabla}}{\partial x} \cdot (\underline{\alpha_3} \cdot \vec{\nabla} h)$$
$$+ \sum_{i,j=x,y} \alpha_{4ij} \frac{\partial^2}{\partial i^2} \frac{\partial^2}{\partial j^2} h + \frac{\partial h}{\partial x} \cdot \vec{\nabla} \cdot (\underline{\alpha_5} \cdot \vec{\nabla} h)$$
$$+ \vec{\nabla} h \cdot (\underline{\alpha_6} \cdot \vec{\nabla} h) \Bigg], \tag{5}$$

For this formula, they expanded only to the lowest nonlinear order in h by approximating all ripples to have small slopes. In this expression, the parameter α_0 defines the excavation rate of a flat surface and $\underline{\alpha_i} = \text{diag}(\alpha_{ix}, \alpha_{iy})$ are 2×2 diagonal matrices for $i = 2, 3, \overline{5}, 6$. The local redeposition velocity is described as [64]

$$\Gamma_{ad} = \kappa_0 \Bigg[R - R_{eq} \Bigg(1 - \zeta_{2x} \frac{\partial^2 h}{\partial x^2} - \zeta_{2y} \frac{\partial^2 h}{\partial y^2} \Bigg) \Bigg]. \tag{6}$$

The relaxation is presumed to be an adatom diffusion process in the spirit of the model of Herring and Mullins [22,23]. Here, κ_0 is the average nucleation rate for a flat surface, R_{eq} is the thickness of the dynamic layer in an equilibrium state without ion irradiation, and $\zeta_{2x}, \zeta_{2y} \geq 0$ describe the variation in the nucleation rate with the surface curvatures.

In a first step, MCC calculated the time evolution of an initially flat surface and then added periodic perturbations

in a linear stability analysis, deriving a dispersion relation ω_k (where k is the wave vector of a perturbation) [29,64]. Here, ω_k has two complex solutions, ω_k^+ and ω_k^-. Their real part expresses the evolution of the amplitude, while the imaginary part describes the lateral (in-plane) propagation of the perturbation. For an approximation for large wavelengths, only ω_k^+ describes nontrivial dynamics. The velocity for lateral propagation of periodic features of a wavelength λ is then [64]

$$v(\lambda) = -\frac{\text{Im}\left(\omega_{k_x}^+\right)}{k_x} \equiv A + B\frac{1}{\lambda^2}, \qquad (7)$$

where

$$A = \alpha_0 \alpha_{1x} \varphi, \qquad (8a)$$

$$B = 4\pi^2 \alpha_0 \left[\alpha_{1x}\left(\frac{(1-\varphi)\cdot D}{\kappa_0} - \varphi\,\zeta_{2x}R_{eq}\right) - \varphi\,\alpha_{3x} \right]. \qquad (8b)$$

Here, D is the diffusion coefficient for mobile atoms on the surface. The parameters α_0, α_{1x}, and α_{3x} are related to the specific shape of the energy deposition in the solid [64]

$$\alpha_0 = v_0,$$
$$\alpha_{1x} = -\gamma_x/v_0, \qquad (9)$$
$$\alpha_{3x} = -\Omega_1/v_0.$$

Here, v_0 is the erosion velocity perpendicular to the global surface; γ_x and Ω_1 are determined by assuming a Gaussian energy deposition profile [20,21]; they relate to the average depth of energy deposition of the ions a, the longitudinal and transverse straggling widths σ and μ, respectively, and the ions' incidence angle θ [10]. The specific functional dependences of γ_x and Ω_1 on these parameters (a, σ, μ, and θ) are detailed in the appendix.

B. Comparison of experimental results with predictions of the two-field model

In the following, the predictions from the model outlined above will be compared with the results obtained experimentally in terms of the dependence of the propagation velocity v on the ripple wavelength (Fig. 6). Specifically, the parameters A and B in Eq. (8) will be computed and compared with the corresponding values $A_{\text{exp}} = (61.9 \pm 1.9)$ nm/$(10^{17}$ ions cm$^{-2})$ and $B_{\text{exp}} = (2.73 \pm 0.24) \times 10^6$ nm^3/$(10^{17}$ ions cm$^{-2})$ derived from the fit in Fig. 6. Applying the ion flux $f = 3.1 \times 10^{14}$ cm^{-2} s^{-1}, $A_{\text{exp}}\,f = 0.19$ nm/s and $B_{\text{exp}}\,f = 8.6 \times 10^3$ nm^3/s; these values are directly related to A and B in Eq. (8). From the total fluence 2.4×10^{18} ions cm^{-2}, the ion flux density, and the final crater depth of 1.4 μm determined by AFM, the vertical erosion velocity is obtained $v_0 = a_0 = -0.18$ nm/s.

In Figure 8(a), values of $A = \varphi\alpha_0\alpha_{1x}$ in Eq. (8a) computed by means of Eq. (9) are plotted as a function of the ratio a/σ, with $a/\mu = 1.3\,a/\sigma$ and φ as a parameter ($\varphi = 0.1$, 0.3, 0.5, 0.8, and 1). The horizontal line gives the experimentally derived value $A_{\text{exp}}\,f = 0.19$ nm/s. The choice $\sigma/\mu = 1.3$ is derived from the spatial moments of damage distributions [68]. Figure 8(a) shows that, depending on the
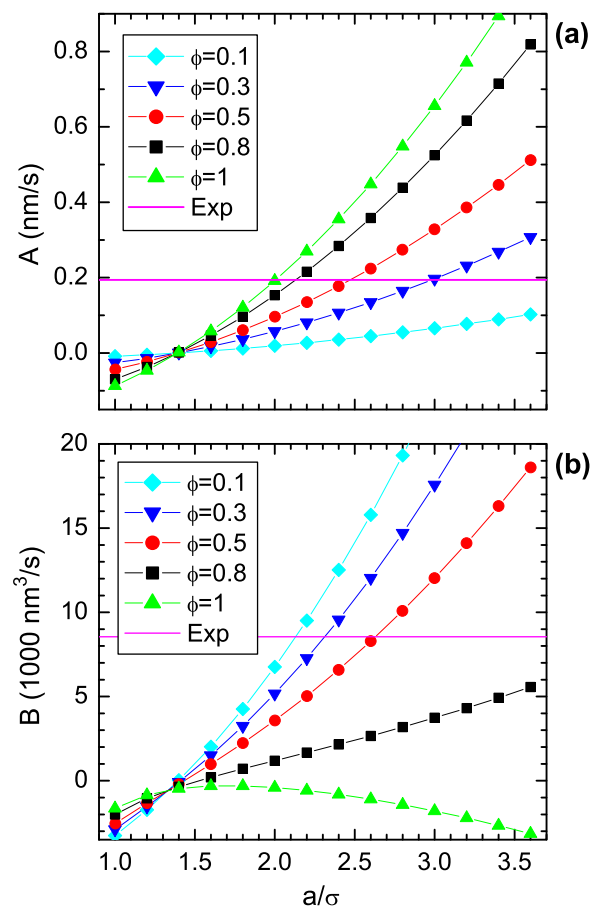

FIG. 8. (Color online) (a) The parameter A in Eq. (8a) calculated as a function of the ratio a/σ for various values of φ with $a/\mu = 1.3\,a/\sigma$. (b) The value of B in Eq. (11) as a function of the ratio a/σ for various values of φ with $a/\mu = 1.3\,a/\sigma$, $a = 20$ nm, $\gamma = 1$ J/m^2, $d = 10$ nm, $\eta/\tau_R = 10^7$ Pa. In both graphs, the horizontal line gives the experimental values derived from the fit in Fig. 6.

magnitude of φ, the calculated values of A agree only within a rather specific range of a/σ ($\sim 2-3$) with the experimental data. This range appears to be appropriate also in the frame of these damage distributions [68]. Using for the computations $a/\mu = a/\sigma$ instead causes a shift of the possible range of a/σ to only slightly larger values ($\sim 2.2-3.2$). For comparison, the simulation code SRIM-2008 [69] computes for the present experimental conditions the following ion range parameters for the pure glass sample: $a = 17$ nm, $\sigma = 7.5$ nm, and $\mu = 7.3$ nm. Including the incorporated Ga atoms (with an atomic fraction of 0.15) reduces the ranges by about 10%. While these are seen to be in agreement with what is found from Fig. 8(a), the actual energy deposition distribution might not be described accurately enough by them in order to select a specific value of φ in this way. Nonetheless, the quantitative agreement of $A_{\text{exp}}\,f$ derived from the experiment with the computed theoretical magnitude of A in Eq. (8a) corroborates the validity of the model by MCC [64].

In a similar vein, the parameter B in Eq. (8b) can be compared to the value of $B_{\text{exp}}\,f$ obtained in the experiment. Apart from the parameters α_{1x} and α_{3x} related to the energy deposition of the ion beam, several additional parameters

governing diffusive processes are required to compute B; according to [64], $R_{eq} \sim 1$ nm, $\zeta_{2x} \sim 4$ nm, $D \sim 10^5$ nm^2 s^{-1}, and $\kappa_0 \sim 10^9$ s^{-1} are proposed. It should be pointed out that the diffusion coefficient D refers to Si diffusion under noble-gas ion bombardment. Unfortunately, we are not aware of any data for Ga bombardment of SiO$_2$. Employing these values, the magnitude of B turns out to be much too small as compared to the corresponding experimental data. In particular, the ratio $D/\kappa_0 \sim 10^{-4}$ nm^2 makes this term in Eq. (8b) negligibly small, irrespective of the choice of φ. In fact, using those parameter to compute B yields values that are more than an order of magnitude lower than the experimental one. An agreement with the experimental data could only be achieved by choosing a value of $D/\kappa_0 \sim 2 \times 10^3$ nm^2, clearly unrealistically large in view of the above-mentioned parameters.

As an alternative to thermal surface diffusion processes, roughness on amorphous surfaces can relax by viscous flow [17,18,70]; limited to a thin surface layer, it may contribute to the height evolution. In the presence of an ion beam, the effective fluidity in this film can be many orders of magnitude larger than that in the bulk, a phenomenon known as radiation-induced viscous flow. The enhanced flow is believed to be caused by point defects or other damage induced by the energetic ion [71] and has been observed in a wide range of materials bombarded with kiloelectron volt to megaelectron volt ions [17,18,72,73]. For low-energy ions, the enhanced viscous flow is confined to a thin surface layer d. In most cases, d is approximately equal to the range of the ion a. The evolution kinetics of the surface-confined viscous flow was solved by Orchard [74] for the flow of a thin layer of liquid on a stiff substrate. The relevant relaxation rate in this situation would be a scaling with $\gamma d^3/\eta$, where γ is the surface free energy, and η is the surface viscosity. To replace adatom diffusion by viscous surface flow, the corresponding parameters have to be identified [64,74]

$$\frac{\partial h}{\partial t} = -R_{eq} \cdot D \cdot \zeta_2 \cdot \nabla^4 h,$$
$$\frac{\partial h}{\partial t} = -\frac{\gamma \cdot d^3}{\eta} \cdot \nabla^4 h. \tag{10}$$

A comparison of the units in Eq. (10) leads to the following substitutions: $R_{eq} \equiv d$, $\zeta_2 \equiv d$, $D \equiv d\gamma/\eta$. Instead of Eq. (8b), the alternative formula for B in Eq. (7) is then

$$B = 4\pi^2 \alpha_0 \left[\alpha_{1x} \left(\frac{(1-\varphi) \cdot \gamma \cdot \tau_R \cdot d}{\eta} - \varphi \cdot d^2 \right) - \varphi \cdot \alpha_{3x} \right]. \tag{11}$$

The thickness d of the viscous layer is comparable to the depth up to which most of the collision events take place. SRIM-2008 simulations [69] suggest d to be in the range of 5 to 20 nm. The viscosity η of the material during ion bombardment is reduced by a factor related to the flux. With a flux of 3.1 $\times 10^{14}$ cm^{-2} s^{-1}, η is of the order of magnitude of 10^9 Pa s [75]. The relaxation time τ_R for viscous surface flow during ion-beam irradiation was measured to be of the order of 1 to 100 s [70,76–78]. The surface energy γ is of the order of magnitude of 0.3 to 1 J/m^2 [44,70].

Similar to Fig. 8(a), values of B in Eq. (11) are plotted in Figure 8(b) as a function of the ratio a/σ, with $a/\mu =$

1.3 a/σ and φ as a parameter ($\varphi = 0.1$, 0.3, 0.5, 0.8, and 1). For the other parameters, the following values were chosen: $\gamma = 1$ J/m^2, $d = 10$ nm, $\eta/\tau_R = 10^7$ Pa. The horizontal line gives the experimentally derived value $B_{exp} f = 8.6 \times 10^3$ nm^3/s. For the specific range of a/σ ($\sim 2-3$) derived from the computation of A above, the calculated values of B are found to agree with the experimental data only for a limited range of φ ($\sim 0.1-0.6$). As the comparison presented in Fig. 8(a) appears to restrict φ to values ≥ 0.3, both datasets combined would indicate that an agreement of the theoretical parameters A and B with the experimental data is obtained only for roughly $0.3 \leq \varphi \leq 0.6$. This finding implies that both contributions, surface erosion by sputtering and relaxation by viscous flow, have to be active to a substantial extent. For these conditions, a quantitative agreement of the experimentally observed dependence of the ripple propagation velocity on the ripple wavelength (Fig. 6) with the prediction of the model of MCC [64] is found and strongly supports its validity.

There are clearly some uncertainties associated with the parameters employed in the foregoing evaluations. For example, α_{1x} and α_{3x} are calculated under the assumption that the contours of equal energy deposition are ellipsoids of revolution. Their specific shape and size are, however, not known precisely. Furthermore, experimental parameters of viscous flow during ion bombardment are still sparse and limited to specific irradiation conditions.

For completeness, it is mentioned that a wavelength-dependent propagation velocity of ripples was predicted also in a model for the effect of stress on thin amorphous films that develop on ion-irradiated silicon, based on the mechanism of ion-induced anisotropic plastic flow [28]. The functional form of this dependence is $v \propto C/\lambda^2$; the constant C depends on the thickness of the film, the ions' incidence angle and flux, and the magnitude of strain induced per ion. This model predicts stationary ripples for large wavelengths, contrary to Eq. (7) and the findings of this paper. In fact, the experimental data in Fig. 6 cannot be fitted by a relation such as $v \propto C/\lambda^2$.

A final point worth considering is the possible influence of the implanted Ga atoms in the near-surface region of the specimen. Several detailed experiments [79–86] have shown that the presence of (metallic) impurities on the surface can have a quite pronounced effect on ripple formation. For example, ripples do not form when Si is bombarded at small angles of incidence unless impurities are deposited concurrently [87]. However, it is not clear whether implanted species will have the same effect on ripple structures than atoms being deposited onto the surface.

In this context, it is definitely relevant, however, to point out that the assumption that rare-gas ion irradiation (and incorporation) as employed frequently will have no influence on the formation and evolution of nanostructures appears to be not *a priori* justified. In fact, recent work [88] for 40 keV Xe$^+$ bombardment of Si has shown the formation of gas-filled bubbles over the penetration depth of the ions, with sizes of up to 7 nm and a Xe concentration of 20 at%. This stationary state was reached at a fluence (1.5×10^{16}/cm^2) much lower than those for which ripple formation is often observed. With continuing ion bombardment, these cavities will be opened. Clearly, such processes could constitute a massive

modification of the surface region. Ideally, the distribution of incorporated ion species (both for Ga and for rare-gas ions) should be determined concurrently with the formation of ion-induced nanostructures.

V. CONCLUSIONS

Periodic patterns of different wavelengths (from 150 to 750 nm) on glass surfaces were bombarded by 30 keV Ga$^+$ ions at an incidence angle of 52°. The irradiation results in the formation of ripple structures with wavelengths λ identical with those of the original pattern. Their evolution was monitored *in situ* in a dual-beam FIB system. (At this point, it is not clear if the initial prepattern aspect ratios may have an influence on the further pattern evolution, an aspect that warrants future investigations.) The ripples were found to propagate across the surface in a direction which corresponds to the projection of the ion beam onto the surface. The propagation velocity was found to scale with $A + B/\lambda^2$. This dependence is in accordance with the predictions of a theoretical two-field continuum model of ripple formation which treats the surface as being composed of a thin layer of mobile species on an immobile substrate. The experiment therefore supports that theoretical approach. However, to obtain a full quantitative agreement, the smoothing term(s) in the model cannot be due to surface diffusion of mobile adatoms. By contrast, the presence of a viscous flow in a thin surface layer can explain the experimental findings in a quantitative way. It should be pointed out, however, that this theoretical model [64] is based on a small-slope approximation, whereas experimentally large slopes are present in the ripple structures. On the other hand, the fact that, for ripples with initial wavelengths between 350 and 750 nm, these remain the same with ion bombardment might indicate that different (and larger) slopes are not decisive.

APPENDIX

The values of γ_x and Ω_1 in Eq. (9) are determined by the average energy deposition depth of the ions a, the longitudinal straggling σ and transverse straggling μ, and the ions' incidence angle θ, assuming a Gaussian ellipsoid-shaped profile of energy deposition. The specific functional dependence of γ_x and Ω_1 on these parameters is as follows [10]:

$$\gamma_x = v_0 \frac{s\, a_\sigma^2}{c\, g^2} \cdot \left[a_\mu^2\, c^2 \left(a_\sigma^2 - 1 \right) - a_\sigma^2\, s^2 \right], \qquad \text{(A1)}$$

$$\Omega_1 = -v_0 \frac{3}{6} \frac{s\, a^2}{c\, a_\mu^2\, g^2} \cdot \left[g^2 - g\, a_\sigma^4\, c^2 \right.$$
$$\left. - \left(a_\mu^2 - a_\sigma^2 \right) c^2 \left(g + a_\sigma^4\, s^2 \right) \right], \qquad \text{(A2)}$$

with $s \equiv \sin\theta$, $c \equiv \cos\theta$, $a_\sigma \equiv a/\sigma$, $a_\mu \equiv a/\mu$, and $g \equiv a_\sigma^2 s^2 + a_\mu^2 c^2$. More recently, Bradley [89] derived a slightly different expression for Ω_1

$$\Omega_1 = -v_0 \frac{1}{6} \frac{s\, a^2 a_\sigma^2}{c\, g^4} \cdot \left[3g \left(g + a_\sigma^4\, s^2 \right) \right.$$
$$\left. - a_\sigma^2\, a_\mu^2\, c^2 \left(3g + a_\sigma^4\, s^2 \right) \right]. \qquad \text{(A3)}$$

Numerically, the difference between Eqs. (A2) and (A3) is found to be small for the present parameters and has a negligible influence on the value of B in either Eq. (8b) or Eq. (11).

[1] G. Carter and J. S. Colligon, *Ion Bombardment of Solids* (Heineman, London, 1968).

[2] M. Nastasi, J. W. Mayer, and J. K. Hirvonen, *Ion Solid Interactions: Fundamentals and Applications* (Cambridge University Press, Cambridge, 1996).

[3] G. Carter, B. Navinšek, and J. L. Whitton, in *Sputtering by Particle Bombardment II*, edited by R. Behrisch (Springer, Berlin, 1983), p. 231.

[4] H. Gnaser, *Low-Energy Ion Irradiation of Solid Surfaces* (Springer, Berlin, 1999).

[5] S. Facsko, T. Dekorsy, C. Koerdt, C. Trappe, H. Kurz, A. Vogt, and H. L. Hartnagel, Science **285**, 1551 (1999).

[6] F. Frost, A. Schindler, and F. Bigl, Phys. Rev. Lett. **85**, 4116 (2000).

[7] S. Rusponi, G. Costantini, C. Boragno, and U. Valbusa, Phys. Rev. Lett. **81**, 2735 (1998).

[8] F. Frost, B. Ziberi, A. Schindler, and B. Rauschenbach, Appl. Phys. A **91**, 551 (2008).

[9] G. Carter, J. Phys. D: Appl. Phys. **34**, R1 (2001).

[10] M. A. Makeev, R. Cuerno, and A.-L. Barabási, Nucl. Instrum. Methods B **197**, 185 (2002).

[11] U. Valbusa, C. Boragno, and F. Buatier de Mongeot, J. Phys. Condens. Matter **14**, 8153 (2002).

[12] M. J. Aziz, K. Dan. Vidensk. Selsk. Mat. Fys. Medd. **52**, 187 (2006).

[13] W. L. Chan and E. Chason, J. Appl. Phys. **101**, 121301 (2007).

[14] J. Muñoz-García, L. Vázquez, R. Cuerno, J. A. Sánchez-García, M. Castro, and R. Gago, in *Towards Functional Nanomaterials*, Z. M. Wang, ed. (Springer, New York, 2009), p. 323.

[15] S. W. MacLaren, J. E. Baker, N. L. Finnegan, and C. M. Loxton, J. Vac. Sci. Technol. A **10**, 468 (1992).

[16] S. Facsko, H. Kurz, and T. Dekorsy, Phys. Rev. B **63**, 165329 (2001).

[17] E. Chason, T. M. Mayer, B. K. Kellerman, D. T. McIlroy, and A. J. Howard, Phys. Rev. Lett. **72**, 3040 (1994).

[18] T. M. Mayer, E. Chason, and A. J. Howard, J. Appl. Phys. **76**, 1633 (1994).

[19] R. M. Bradley and J. M. E. Harper, J. Vac. Sci. Technol. A **6**, 2390 (1988).

[20] P. Sigmund, Phys. Rev. **184**, 383 (1969).

[21] P. Sigmund, J. Mater. Sci. **8**, 1545 (1973).

[22] C. Herring, J. Appl. Phys. **21**, 301 (1950).

[23] W. W. Mullins, J. Appl. Phys. **30**, 77 (1959).

[24] C. C. Umbach, R. L. Headrick, and K.-C. Chang, Phys. Rev. Lett. **87**, 246104 (2001).

[25] R. Cuerno and A.-L. Barabási, Phys. Rev. Lett. **74**, 4746 (1995).

[26] N. V. Medhekar, W. L. Chan, V. B. Shenoy, and E. Chason, J. Phys.: Condens. Matter **21**, 224021 (2009).

[27] G. Carter, Surf. Interface Anal. **25**, 952 (1997).

[28] S. A. Norris, Phys. Rev. B **86**, 235405 (2012).

[29] M. Castro, R. Cuerno, L. Vázquez, and R. Gago, Phys. Rev. Lett. **94**, 016102 (2005).

[30] J. Muñoz-García, M. Castro, and R. Cuerno, Phys. Rev. Lett. **96**, 086101 (2006).

[31] M. Castro and R. Cuerno, Appl. Surf. Sci. **258**, 4171 (2012).

[32] S. Facsko, T. Bobek, A. Stahl, H. Kurz, and T. Dekorsy, Phys. Rev. B **69**, 153412 (2004).

[33] E. Chason and V. Shenoy, Nucl. Instrum. Methods B **272**, 178 (2012).

[34] G. Carter and V. Vishnyakov, Phys. Rev. B **54**, 17647 (1996).

[35] M. Moseler, P. Gumbsch, C. Casiraghi, A. C. Ferrari, and J. Robertson, Science **309**, 1545 (2005).

[36] B. Davidovitch, M. J. Aziz, and M. P. Brenner, Phys. Rev. B **76**, 205420 (2007).

[37] C. S. Madi, E. Anzenberg, K. F. Ludwig, and M. J. Aziz, Phys. Rev. Lett. **106**, 066101 (2011).

[38] S. A. Norris, J. Samela, L. Bukonte, M. Backman, F. Djurabekova, K. Nordlund, C. S. Madi, M. P. Brenner, and M. J. Aziz, Nature Commun. **2**, 276 (2011).

[39] N. Kalyanasundaram, M. Ghazisaeidi, J. B. Freund, and H. T. Johnson, Appl. Phys. Lett **92**, 131909 (2008).

[40] M. Z. Hossain, J. B. Freund, and H. T. Johnson, J. Appl. Phys. **111**, 103513 (2012).

[41] S. A. Norris, J. Samela, M. Vestberg, K. Nordlund, M. J. Aziz, Nucl. Instrum. Methods B **318**, 245 (2014).

[42] S. Habenicht, K. P. Lieb, J. Koch, and A. D. Wieck, Phys. Rev. B **65**, 115327 (2002).

[43] H. H. Chen, O. A. Urquidez, S. Ichim, L. H. Rodriquez, M. P. Brenner, and M. J. Aziz, Science **310**, 294 (2005).

[44] P. F. A. Alkemade, Phys. Rev. Lett. **96**, 107602 (2006).

[45] Q. Wei, J. Lian, L. A. Boatner, L. M. Wang, and R. C. Ewing, Phys. Rev. B **80**, 085413 (2009).

[46] W. J. MoberlyChan, J. Phys. Condens. Matter **21**, 224013 (2009).

[47] H. Gnaser, Pure Appl. Chem. **83**, 2003 (2011).

[48] H. Gnaser, B. Reuscher, and A. Zeuner, Nucl. Instrum. Methods B **285**, 142 (2012).

[49] H. Hofsäss, K. Zhang, H. G. Gehrke, and C. Brüsewitz, Phys. Rev. B **88**, 075426 (2013).

[50] I. Koponen, M. Hautala, and O.-P. Sievänen, Phys. Rev. Lett. **78**, 2612 (1997).

[51] E. O. Yewande, A. K. Hartmann, and R. Kree, Phys. Rev. B **71**, 195405 (2005).

[52] E. Chason, W. L. Chan, and M. S. Bharathi, Phys. Rev. B **74**, 224103 (2006).

[53] M. Joe, C. Choi, B. Kahng, and J.-S. Kim, Appl. Phys. Lett. **91**, 233115 (2007).

[54] J.-H. Kim, M. Joe, S.-P. Kim, N.-B. Ha, K.-R. Lee, B. Kahng, and J.-S. Kim, Phys. Rev. B **79**, 205403 (2009).

[55] A. Keller and S. Facsko, Phys. Rev. B **82**, 155444 (2010).

[56] J. Völlner, B. Ziberi, F. Frost, and B. Rauschenbach, J. Appl. Phys. **109**, 043501 (2011).

[57] J.-H. Kim, N.-B. Ha, J.-S. Kim, M. Joe, K.-R. Lee, and R. Cuerno, Nanotechnology **22**, 285301 (2011).

[58] J.-H. Kim, J.-S. Kim, J. Muñoz-García, and R. Cuerno, Phys. Rev. B **87**, 085438 (2013).

[59] H. Gnaser, A. Brodyanski, and B. Reuscher, Surf. Interf. Anal. **40**, 1415 (2008).

[60] A. Cuenat, H. B. George, K.-C. Chang, J. M. Blakely, and M. J. Aziz, Adv. Mater. **17**, 2845 (2005).

[61] S. Ichim and M. J. Aziz, J. Vac. Sci. Technol. B **23**, 1068 (2005).

[62] T. Aste and U. Valbusa, Physica A **332**, 548 (2004).

[63] T. Aste and U. Valbusa, New J. Phys. **7**, 122 (2005).

[64] J. Muñoz-García, R. Cuerno, and M. Castro, Phys. Rev. B **78**, 205408 (2008).

[65] J. Muñoz-García, R. Cuerno, and M. Castro, J. Phys. Condens. Matter **21**, 224020 (2009).

[66] R. Cuerno, M. Castro, J. Muñoz-García, R. Gago, and L. Vázques, Nucl. Instrum. Methods B **269**, 894 (2011).

[67] J. Muñoz-García, R. Gago, L. Vázquez, J. A. Sánchez-García, and R. Cuerno, Phys. Rev. Lett **104**, 026101 (2010).

[68] K. B. Winterbon, P. Sigmund, and J. B. Sanders, K. Dan. Vidensk. Selsk. Mat. Fys. Medd. **37**(14), 1 (1970).

[69] Available at: http://www.srim.org.

[70] S. G. Mayr and R. S. Averback, Phys. Rev. Lett. **87**, 196106 (2001).

[71] S. G. Mayr, Y. Ashkenazy, K. Albe, and R. S. Averback, Phys. Rev. Lett. **90**, 055505 (2003).

[72] C. A. Volkert, J. Appl. Phys. **70**, 3521 (1991).

[73] S. Vauth and S. G. Mayr, Phys. Rev. B **75**, 224107 (2007).

[74] S. E. Orchard, Appl. Sci. Res. A **11**, 451 (1962).

[75] M. L. Brongersma, E. Snoeks, and A. Polman, Appl. Phys. Lett. **71**, 1628 (1997).

[76] K. Otani, X. Chen, J. W. Hutchinson, J. F. Chervinsky, and M. J. Aziz, J. Appl. Phys. **100**, 023535 (2006).

[77] M. L. Brongersma, E. Snoeks, T. van Dillen, and A. Polman, J. Appl. Phys. **88**, 59 (2000).

[78] H. B. George, Y. Tang, X. Chen, J. Li, J. W. Hutchinson, J. A. Golovchenko, and M. J. Aziz, J. Appl. Phys. **108**, 014310 (2010).

[79] G. Ozaydin, A. S. Özcan, Y. Wang, K. F. Ludwig, H. Zhou, R. L. Headrick, and D. P. Siddons, Appl. Phys. Lett. **87**, 163104 (2005).

[80] H. Hofsäss and K. Zhang, Appl. Phys. A **92**, 517 (2008).

[81] J. Zhou and M. Lu, Phys. Rev. B **82**, 125404 (2010).

[82] S. Macko, F. Frost, B. Ziberi, D. F. Förster, and T. Michely, Nanotechnol. **21**, 085301 (2010).

[83] K. Zhang, M. Brötzmann, and H. Hofsäss, New J. Phys. **13**, 013033 (2011).

[84] M. Cornejo, B. Ziberi, C. Meinecke, D. Hirsch, J. W. Gerlach, T. Höche, F. Frost, and B. Rauschenbach, Appl. Phys. A **102**, 593 (2011).

[85] A. Redondo-Cubero, R. Gago, F. J. Palomares, A. Mücklich, M. Vinnichenko, and L. Vázquez, Phys. Rev. B **86**, 085436 (2012).

[86] H. Hofsäss, K. Zhang, A. Pape, O. Bobes, and M. Brötzmann, Appl. Phys. A **111**, 653 (2013).

[87] S. Macko, F. Frost, M. Engler, D. Hirsch, T. Höche, J. Grenzer, and T. Michely, New J. Phys. **13**, 073017 (2011).

[88] K. Wittmaack and H. Oppolzer, Nucl. Instrum. Methods B **269**, 380 (2011).

[89] R. M. Bradley, Phys. Rev. B **84**, 075413 (2011).